**Supporting Information**

**Simulation of Heterogeneous Photooxidation of SO$_2$ and NO$_x$ in the presence of Gobi Desert Dust Particles under Ambient Sunlight**

Zechen Yu and Myoseon Jang

5    P.O.Box116450, Department of Environmental Engineering Sciences, Engineering School of Sustainable Infrastructure and Environment, University of Florida, Gainesville, FL, USA, 32611

*Correspondence to*: Myoseon Jang (mjang@ufl.edu)

10    Number of Sections: 1

Number of Tables:2

Number of Figures: 8

## Section 1: Chamber experimental procedure and chamber characterization

### Indoor chamber experiment

The indoor chamber experiments were performed in a 2 m$^3$ Teflon indoor chamber equipped with UV lamps (Wavelength: 280nm – 900 nm) (Solarc Systems Inc., FS40T12/UVB). The RH and the concentration of trace gases and dust particles were controlled to variety specific experimental conditions. During the experiment, the gases were continuously measured using a gas chromatography–flam ionization detector (HP–5890 GC–FID) for organic gases, a fluorescence TRS analyzer (Teledyne Model 102E) for $SO_2$, a chemiluminescence NO/NOx analyzer (Teledyne Model T201) for $NO_x$ and a photometric ozone analyser (Model 400E, Teledyne, USA). The suspended particles were continuously measured by a scanning mobility particle sizer (SMPS, TSI 3080, USA) and an Optical Particle Counter (OPC, TSI 3330, USA). The mass concentration of inorganic iron was measured using a Particle–Into–Liquid Sampler (Applikon, ADISO 2081) combined with Ion Chromatography (Metrohm, 761 Compact IC) (PILS–IC).

### Outdoor chamber experiment

The outdoor experiments were conducted using the University of Florida Atmospheric Photochemical Outdoor Reactor (UF–APHOR) dual chambers located on the roof of Black Hall at University of Florida, Gainesville, Florida (latitude/longitude: 29.64185°/-82.347883°). The total volume of the two half-cylinder shaped chamber is 52 m$^3$ each. The surface to volume ratio is 1.65 m$^2$ m$^{-3}$ for each chamber. The chambers are built with 0.13 mm FEP Teflon film. The meteorological parameters (i.e., temperature, relative humidity, sunlight spectrum and sunlight intensity) are monitored simultaneously both inside and outside the chambers using a hygrometer (CR1000 Measurement and Control System, Campbell Scientific) (temperature and humidity), a fibro–optical portable spectrometer (EPP2000, Stellar Net Inc., USA) (sunlight spectrum) and an ultraviolet radiometer (TUVR, Eppley Laboratory Inc.). In addition, the wall loss rate constants of ozone, $SO_2$, $H_2O_2$ and HONO were measured via separate experiments. The rate constant of particle loss to the chamber wall was also measured for Arizona Test Dust (ATD) particles, Gobi Desert Dust (GDD) particles and the ammonia sulfate inorganic seeded aerosol. The typical particle distributions of ATD particles and GDD particles are shown in the Fig. S1.

Before each experiment, the dual chambers were flushed and cleaned by the air purifier system (GC Series, IQ Air Inc.). The background ion concentrations were measured every time before

experiments. Non–reactive $CCL_4$ (400 ppb) was injected into the dual chamber to determine the chamber dilution factor. Due to the chamber dilution, ambient trace gases (i.e., CO, $O_3$, $CH_4$, HCHO and volatile organic compounds) outside the chamber are intruded into the chamber. The estimated concentration of background gases are 1.8 ppb $CH_4$, 18 ppb HCHO, 6 ppb $CH_3CHO$, 0.1 ppb isoprene

5  and 1 ppb HONO. The measurement procedures of gases, inorganic iron concentration and particle distribution were similar to that of indoor chamber experiments. For measuring the total particle mass concentration, the suspended particles were collected on a 13mm diameter Teflon–coated glass fiber filter (Pall Life Science Pallflex, TX40HI20–WW) for 20 minutes. The filter mass difference was measured using a microbalance (MX5, Mettler Toledo, Columbus, OH).
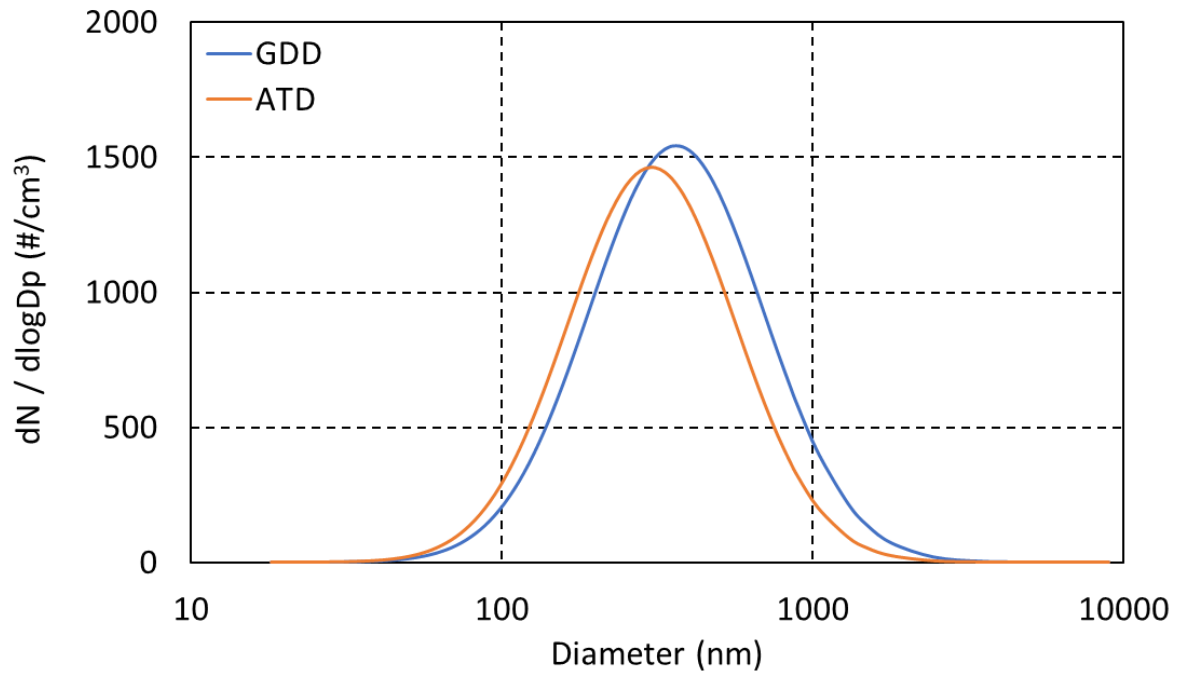
10

Figure S1. Particle size distribution of ATD and GDD dust samples measured during outdoor chamber experiments. The geometric surface area of ATD and GDD particles used in this study were 3.1 and 2.6 $m^2$ $g^{-1}$, respectively.

5

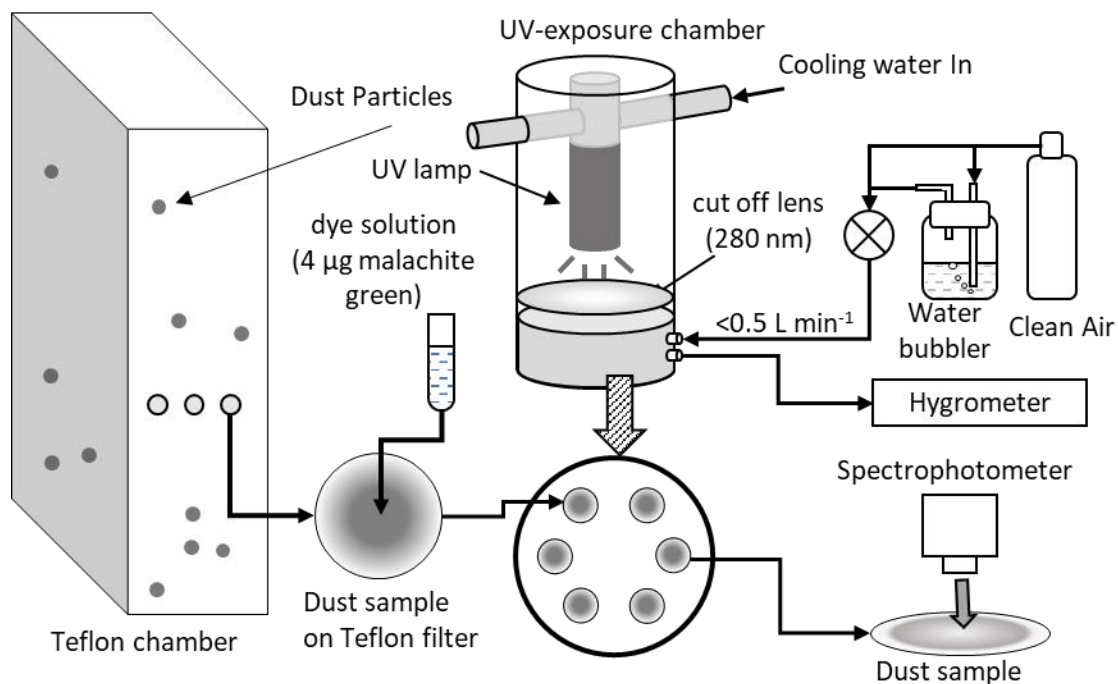Figure S2. The experimental setup to measure the photoactivation capability of dust particles ([M*]$_{dust}$ in Eq. (2)). The dust filter was impregnated with 4 µg malachite green using ethanol solution (0.2 g L$^{-1}$). The humidity inside the exposure box is controlled ranging from less than 10% to 80%.
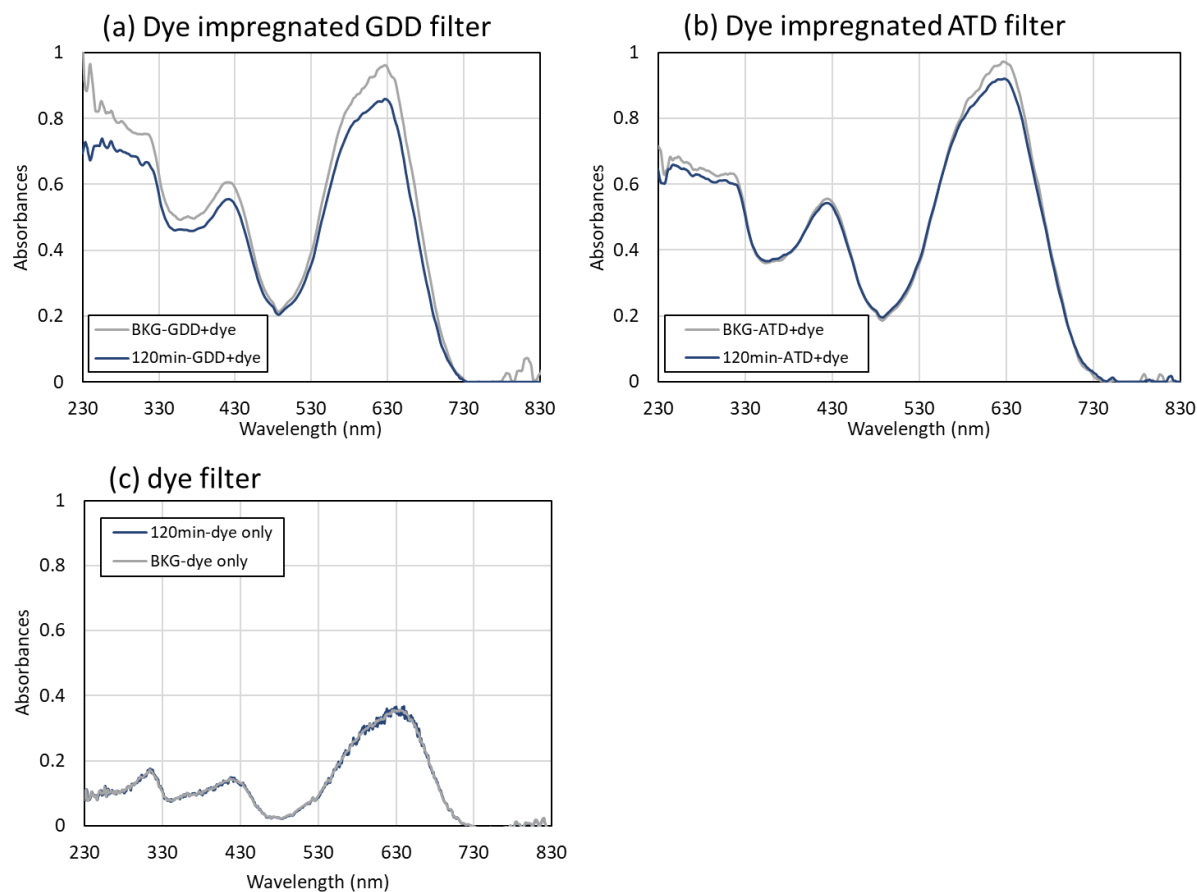
Figure S3: Light absorbance of GDD filter samples that is impregnated with malachite green dye (Fig. S2) before and after irradiation for 120 minutes using UV light (a) The light absorbance of dye impregnated GDD filter samples measured before and after irradiation for 120 minutes using UV light; (b) The light absorbance of dye impregnated ATD filter samples measured before and after irradiation for 120 minutes using UV light. The fabricated flow chamber is operated at 55% RH and the mass of the dust on the filter was 161 µg for ATD filter and 159 µg for the GDD filter. The degradation of dye in the absence of dust particles is negligible (c).
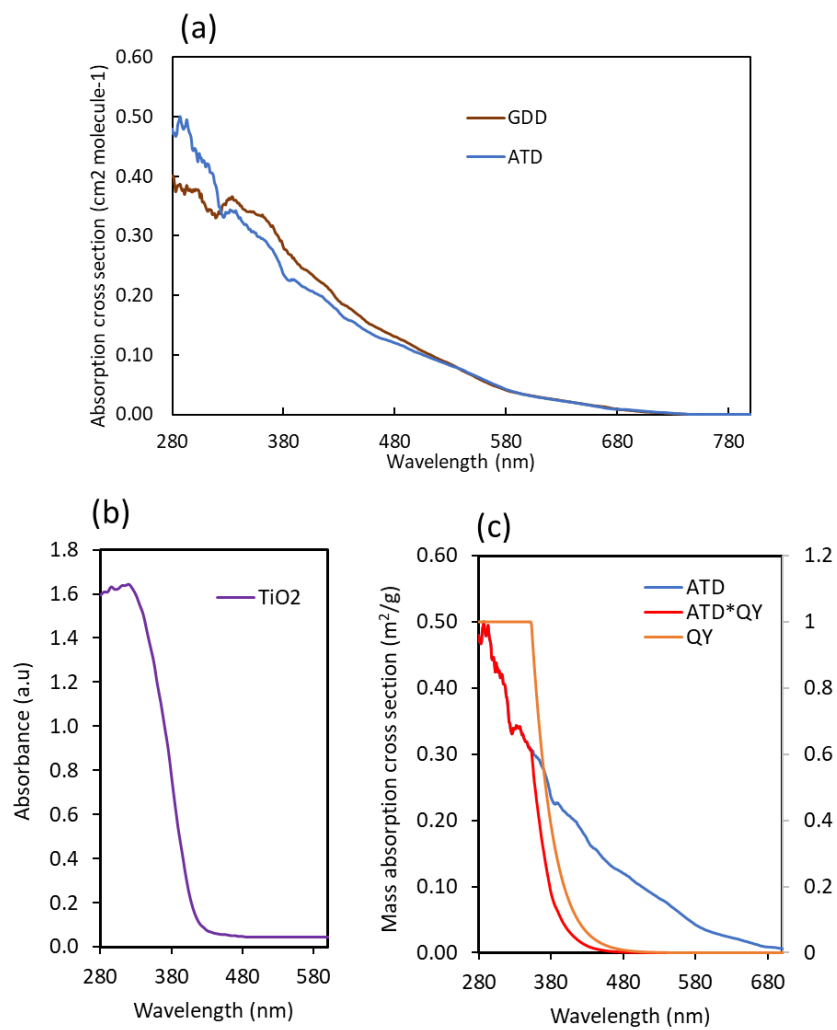
Figure S4 Light absorbance ATD and GDD (a). light absorption of $TiO_2$ and its integration with light absorption of dust particles and quantum yield of (b and c). The light absorbance and quantum yield of ATD are measured and reported in our recent study (Yu et al., 2017).
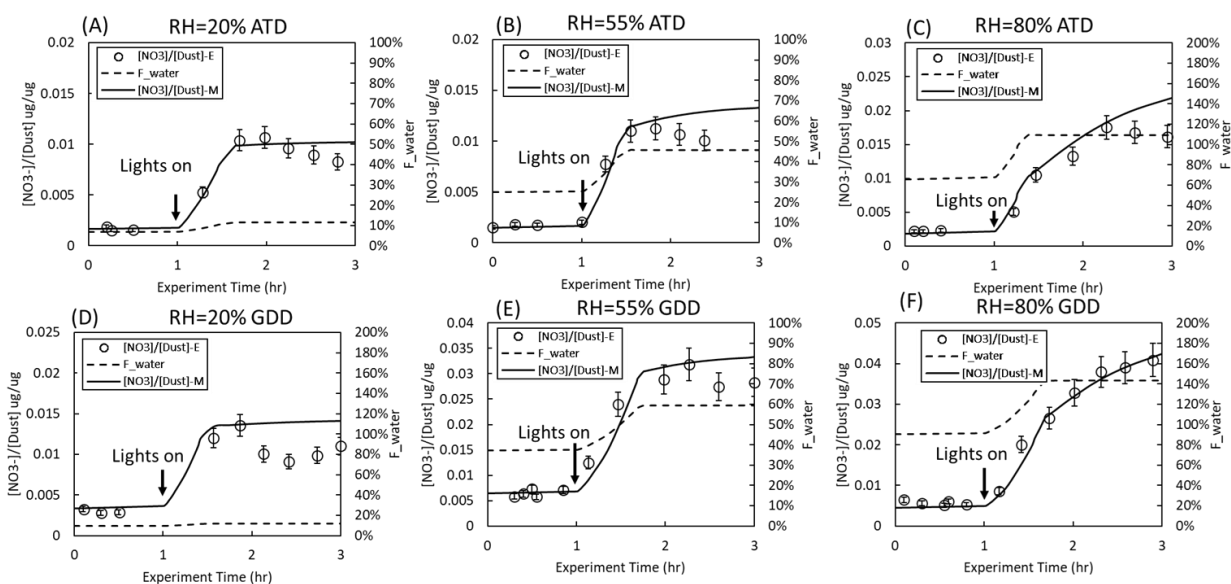
Figure S5. Measurement and simulation of nitrate formation using indoor chamber in the presence of ATD or GDD particle under the three different humidities (20%, 55% and 80%). "Exp" and "Pred" represents the experimental observations and the model predictions, respectively. The error associated with the mass fraction of nitrate on dust particles is ±10% and this originates from PILS-IC measurements. The UV light was on 1 hour after starting the experiment. The details of chamber conditions are shown in Table S1.
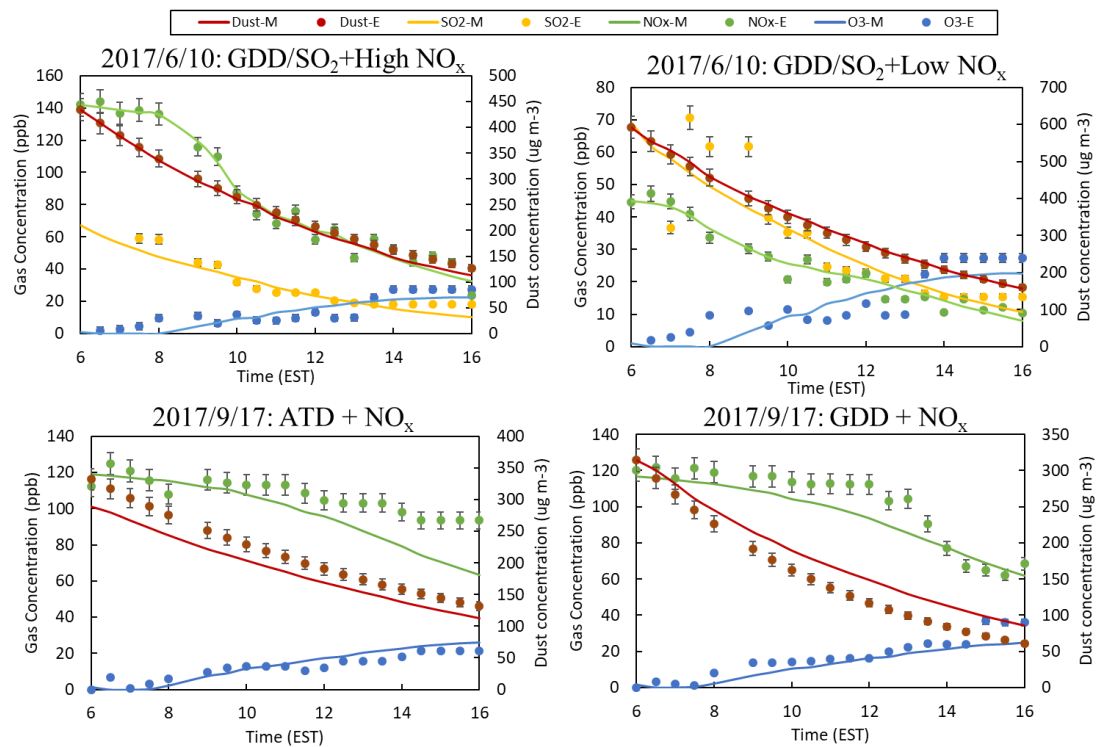
Figure S6. The time profile of concentrations of gaseous compounds and dust mass for the experiments on 2017-6-10 and 2017-9-17 (Table 1).
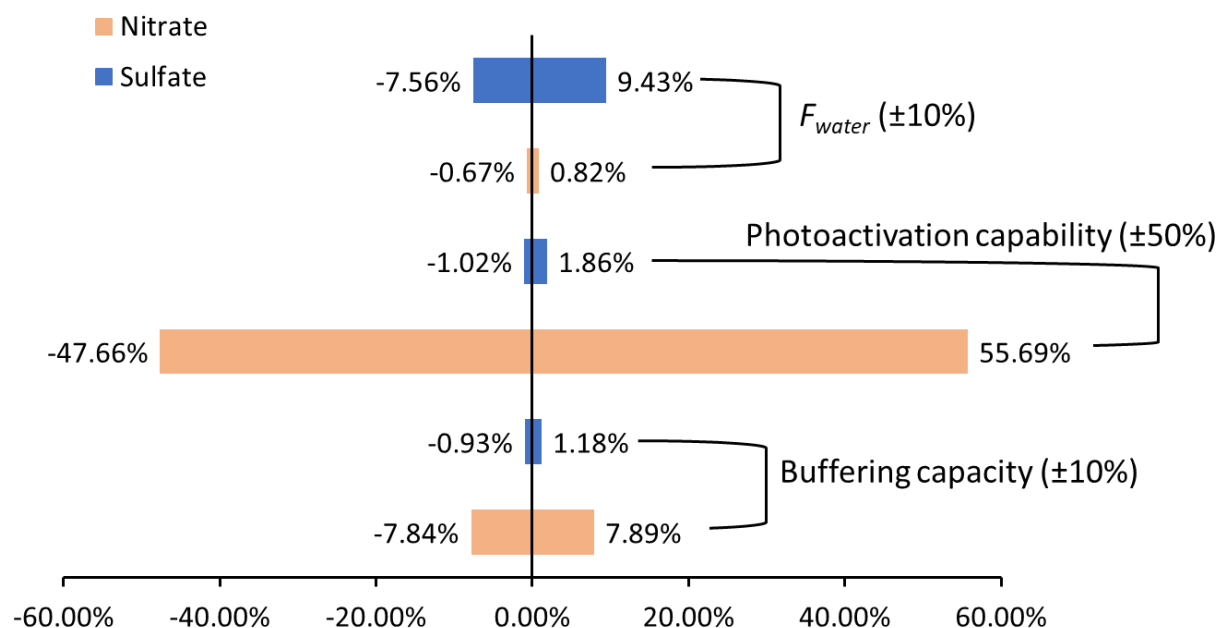
Figure S7. Uncertainties of prediction of sulfate and nitrate due to the variation of $F_{water}$, the photoactivation capability ($[M*]_{dust}$ in Eq. (2)) and the buffering capacity of dust (also see Figure S7). All simulation was performed with 100 µg m$^{-3}$ of initial GDD particles, 2 ppb of initial $O_3$ and 10 ppb isoprene under ambient environmental condition on 23 November 2017. For nitrate production initial 40 ppb $NO_x$ was used and for sulfate formation 40 ppb $SO_2$ and 2 ppb NOx. The simulation was performed without considering the particle loss to the chamber wall.

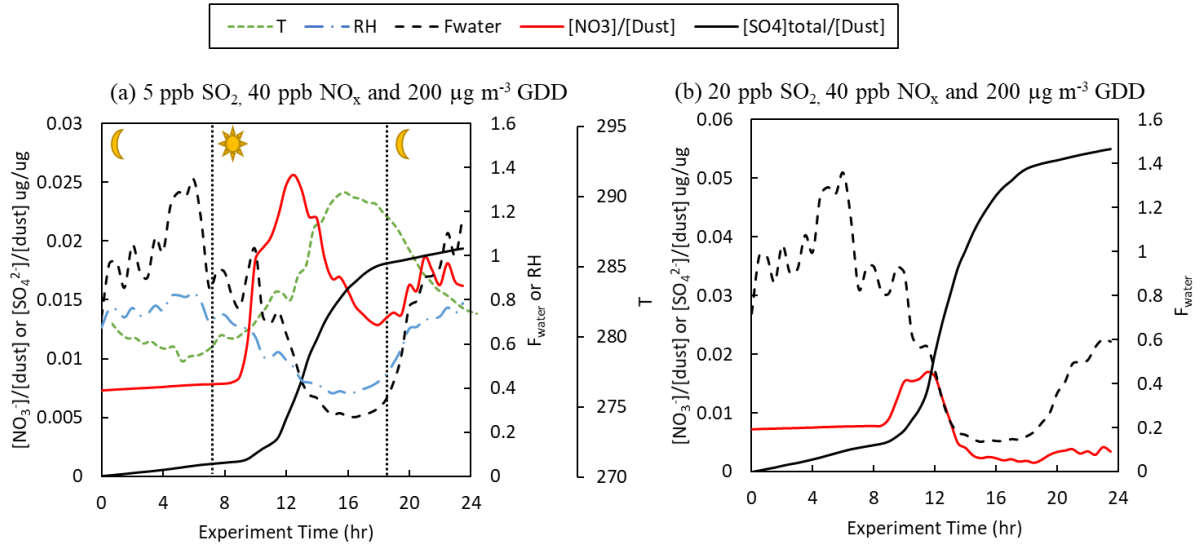Figure S8. 24-hour simulation for the production of nitrate and sulfate using the AMAR model under ambient environmental conditions (January 13, 2016) with (a) 40 ppb $NO_x$ and 5 ppb $SO_2$ in the presence of 200 µg m$^{-3}$ GDD; and (b) 40 ppb $NO_x$ and 20 ppb $SO_2$ in the presence of 200 µg m$^{-3}$ GDD. $F_{water}$ is also predicted in each Figures. The particle loss is not considered in the simulation.

**Table S1.** Experimental conditions for $NO_x$ oxidation in the presence of Gobi Desert dust (GDD) particles using an indoor chamber under different environmental conditions.

| Exp. No[a] | Purpose | Type of particles | Mass conc. of particles[b] ($\mu g\ m^{-3}$)[c] | RH[c] (%) | Temp[c]. (°C) | Initial NO/NO$_2$ conc. (ppb)[c] | Initial O$_3$ conc. (ppb)[c] |
|---|---|---|---|---|---|---|---|
| GDD-1 | RH effect | GDD | 360.1 | 20.8 | 22.8 | 28.1/157.1 | 2.3 |
| GDD-2 | RH effect | GDD | 327.5 | 54.8 | 23.1 | 24.1/135.1 | 1.6 |
| GDD-3 | RH effect | GDD | 596.9 | 80.3 | 23.0 | 36.1/202.1 | 2.1 |
| ATD-1 | RH effect | ATD | 433.4 | 20.3 | 23.1 | 25.1/140.1 | 1.1 |
| ATD-2 | RH effect | ATD | 477.7 | 54.5 | 23.0 | 26.1/145.1 | 3.1 |
| ATD-3 | RH effect | ATD | 404.9 | 80.1 | 22.0 | 49.1/277.1 | 0.7 |

[a] The time profile of the prediction and measurement of nitrate concentration is shown in Fig. S5.
[b] The mass concentrations of GDD particles were calculated from the SMPS data combined with the OPC data. The density of dust particles is 2.65 g cm$^{-3}$, and the particle size distribution was calculated up to 3 µm.
[c] The errors associated with NO, NO$_2$, and O$_3$ were ±12.5%, ±6.9%, and ±0.2%, respectively. The error associated with the dust mass were ±6% based on SMPS and OPC data. The accuracy of the RH and temperature were ±5 % and ±0.5 K, respectively.

**Table S2. Summarized major chemical mechanisms for AMAR model**

| | Reaction | Rate constant [a] | $k_1$ | $k_2$ | $k_3$ | Note[b] |
|---|---|---|---|---|---|---|
| | | *Gas-dust partitioning* [c] | | | | |
| 1 | $SO_2 + Dust \rightarrow SO_2(d) + Dust$ | d | $1\times10^{-8}$ | | | Adams et al., 2005; Huang et al., 2015 |
| 2 | $SO_2(d) \rightarrow SO_2$ | e | $1\times10^{9}$ | 3100 | 0.013 | Adams et al., 2005; Huang et al., 2015 |
| 3 | $O_3 + Dust \rightarrow O_3(d) + Dust$ | d | $1\times10^{-8}$ | | | Michel et al. 2003; Underwood et al. 2001 |
| 4 | $O_3(d) \rightarrow O_3$ | e | $3\times10^{10}$ | 2700 | 0 | Michel et al. 2003; Underwood et al. 2001 |
| 5 | $NO_2 + Dust \rightarrow NO_2(d) + Dust$ | d | $1\times10^{-8}$ | | | Chameides 1984 |
| 6 | $NO_2(d) \rightarrow NO_2$ | e | $1\times10^{10}$ | 2500 | 0 | Chameides 1984 |
| 7 | $HNO_3 + Dust \rightarrow HNO_3(d) + Dust$ | d | $1\times10^{-8}$ | | | Schwartz and White 1981; Schwartz 1984 |
| 8 | $HNO_3(d) \rightarrow HNO_3$ | e | $1\times10^{15}$ | 8700 | 15.4 | Schwartz and White 1981; Schwartz 1984 |
| 9 | $HONO + Dust \rightarrow HONO(d) + Dust$ | d | $1\times10^{-8}$ | | | Becker et al. 1996 |
| 10 | $HONO(d) \rightarrow HONO$ | e | $1\times10^{10}$ | 4900 | 0 | Becker et al. 1996 |
| 11 | $N_2O_5 + Dust \rightarrow HNO_3(d) + Dust$ | d | $7.3\times10^{-3}$ | | | Wagner et al. 2009 |
| | | *Dust phase* | | | | |
| 12 | $Dust + h\upsilon \rightarrow Dust + e\_h$ | | $k_{e\_h}^{j}$[f] | | | this study |
| 13 | $e\_h \rightarrow energy$ | g | $1\times10^{-2}$ | | | Yu et al. 2017 |
| 14 | $e\_h + O_2 \rightarrow OH(d)$ | g | $1.5\times10^{-21}\times F_{water}$ | | | this study |
| 15 | $SO_2(d) \rightarrow SO_4^{2-}(d)$ | g | $5\times10^{-6}$ | | | Yu et al. 2017 |
| 16 | $SO_2(d) + OH(d) \rightarrow SO_4^{2-}(d)$ | g | $1\times10^{-12}$ | | | Yu et al. 2017 |
| 17 | $SO_2(d) + O_3(d) \rightarrow SO_4^{2-}(d) + O_2$ | g | $1\times10^{-13}$ | | | Yu et al. 2017 |
| 18 | $e\_h + O_3(d) \rightarrow OH(d) + O_2$ | g | $1\times10^{-12}$ | | | Yu et al. 2017 |
| 19 | $NO_2(d) \rightarrow NO_3^{-}(d)$ | g | $6\times10^{-5}$ | | | Yu et al. 2017 |
| 20 | $e\_h + NO_2(d) \rightarrow HONO(d)$ | g | $6\times10^{-12}$ | | | Yu et al. 2017 |
| 21 | $HONO(d) + h\upsilon \rightarrow OH(d) + NO$ | | $j_{[HONO]}$ | | | Stockwell and Calvert, 1978; Atkinson et al., 1997 |

| | Reaction | Rate constant [a] | $k_1$ | $k_2$ | $k_3$ | Note[b] |
|---|---|---|---|---|---|---|
| 22 | $NO_2(d) + OH(d) \rightarrow NO_3^-(d)$ | g | $1\times10^{-11}$ | | | Yu et al. 2017 |
| 23 | $NO_3^-(d) + Salt(d) \rightarrow NO_3^-(d\_salt)$ | g | $1\times10^{-12}$ | | | Yu et al. 2017 |
| 24 | $SO_4^{2-}(d) + Salt(d) \rightarrow SO_4^{2-}(d\_salt)$ | g | $5\times10^{-13}$ | | | Yu et al. 2017 |
| 25 | $NO_3^-(d\_salt) + SO_4^{2-}(d)$ $\rightarrow SO_4^{2-}(d\_salt)$ | g | $1\times10^{-13}$ | | | Yu et al. 2017 |

| | Reaction | Rate constant [a] | Note[b] |
|---|---|---|---|
| | | *Wall loss* [i] | |
| 1 | $SO_2 \rightarrow$ | $(1.3RH + 3.3)\times10^{-6}$ | For indoor chamber simulation; measured |
| 2 | $O_3 \rightarrow$ | $7\times10^{-5}$ | For indoor chamber simulation; Chen and Jang, 2012 |
| 3 | $SO_2 \rightarrow$ | $(0.7RH + 1.7)\times10^{-6}$ | For outdoor chamber simulation; estimated |
| 4 | $O_3 \rightarrow$ | $3.5\times10^{-5}$ | For outdoor chamber simulation; estimated |
| 5 | *Dust* $\rightarrow$ | k(dust loss) | Measured for each experiment |
| 6 | $SO_4^{2-}(aq) \rightarrow$ | $5\times10^{-6}$ | Yu et al. 2017 |

[a] The unit of reaction rate constants is $s^{-1}$ for first-order reactions, $cm^3$ molecule$^{-1}$ $s^{-1}$ for second-order reactions and $cm^6$ molecule$^{-2}$ $s^{-1}$ for third order reactions. The unit of the rate constants for the dust sorption reactions is $m^3$ $m^{-2}$ $s^{-1}$.

[b] The reaction rate constants in gaseous phase, inorganic salt seeded aqueous phase and dust phase are previously reported by Yu et al. (2017). The

[c] The unit of dust for the model is mass concentration ($\mu g$ $m^{-3}$). During simulation, the concentration of dust is multiplied by a factor of $2.45\times10^{10}$

5 to have same magnitude with other gaseous species.

[d] Rate constant $k = k_1 \sqrt{8\,R\,T/(\pi\,MW)}\, f_{dust,S\_M} / 4$, where $f_{dust,S\_M}$ is geometric surface area normalized by dust mass ($m^2$ $\mu g^{-1}$), R = 8.314 is the ideal gas constant and MW is the molecule weight of chemical species.

[e] Rate constant $k = k_1 \exp\left(-\frac{k_2}{T}\right)/(F_{water}(1 + k_3/[H^+]))$, where $F_{water}$ is calculated using Eq. (3). $[H^+]$ is the concentration of proton and is dynamically calculated using E–AIM II. (Clegg et al., 1998;Wexler and Clegg, 2002;Clegg and Wexler, 2011).

10 [f] The photoactivation rate contents of GDD is estimated to be 2 times higher than ATD (also see Sect 3.3).

[g] Rate constant $k = k_1$.

[h] Rate constant $k = k_1 \exp(k_2)$.

i The wall loss factors for the model simulation are only valid for the indoor and outdoor chambers used this study. The loss factors of gases and particles may be varied for different chamber systems.

## References

Clegg, S., and Wexler, A. S.: Densities and Apparent Molar Volumes of Atmospherically Important Electrolyte Solutions. 2. The Systems $H^+ - HSO_4 -- SO_4^{2-} - H_2O$ from 0 to 3 mol $kg^{-1}$ as a Function of Temperature and $H^+ - NH_4^+ - HSO_4^- - SO_4^{2-} - H_2O$ from 0 to 6 mol $kg^{-1}$ at 25° C Using a Pitzer Ion Interaction Model, and $NH_4HSO_4^-$ H2O and $(NH_4)_3H(SO_4)^{2-}$ $H_2O$ over the Entire Concentration Range, The Journal of Physical Chemistry A, 115, 3461-3474, 2011.

Clegg, S. L., Brimblecombe, P., and Wexler, A. S.: Thermodynamic model of the system $H^+$-$NH_4^+$-$SO_4^{2-}$-$NO_3^-$-$H_2O$ at tropospheric temperatures, The Journal of Physical Chemistry A, 102, 2137-2154, 1998.

Wexler, A. S., and Clegg, S. L.: Atmospheric aerosol models for systems including the ions $H^+$, $NH_4^+$, $Na^+$, $SO_4^{2-}$, $NO_3^-$, $Cl^-$, $Br^-$, and $H_2O$, Journal of Geophysical Research: Atmospheres, 107, 2002.

Yu, Z., Jang, M., and Park, J.: Modeling atmospheric mineral aerosol chemistry to predict heterogeneous photooxidation of $SO_2$, Atmos Chem Phys, 17, 10001-10017, 2017.